Analysis and Design of Cavity-Coupled Microstrip Couplers and Transitions

David M. Pozar, *Fellow, IEEE*

***Abstract*—This paper describes a full-wave moment-method analysis of an aperture-coupled microstrip coupler using a resonant cavity (rectangular or circular) between the substrate ground planes. Structures of this type are useful for millimeter-wave integrated circuits and phased arrays, as they allow the use of a relatively thick central ground plane to provide isolation, as well as heat dissipation. Both four-port coupler geometries and two-port transitions are treated. Equivalent circuits are derived for each of these problems, and computed results are validated with data from the literature and with independent calculations from commercial computer-aided design (CAD) packages and measured data. These comparisons show that the solutions derived here are accurate and computationally efficient, and have the added advantage over commercial CAD packages in that equivalent-circuit parameters can be obtained directly. The vector Bessel transform is used to derive the required Green's function for the circular cavity.**

***Index Terms*—Aperture coupling, cavity coupling, microstrip couplers.**

I. Introduction

THIS PAPER presents an analysis of a microstrip interconnect geometry that consists of microstrip lines printed on two parallel substrates, and aperture coupled to each end of a resonant cavity located between the substrate ground planes. This structure can be considered as a four-port coupler, but a two-port transition between the two microstrip lines can be formed by terminating each line with an open-circuited stub. A full-wave moment-method solution is used to evaluate the S parameters of the four-port coupler network, and it is shown how equivalent circuits can be derived and used to design a two-port microstrip transition. Both rectangular and circular cavities are considered, and results are compared with previously published data, commercial computer-aided design (CAD) packages, and newly measured data. The required Green's functions for the circular cavity are derived using a vector Bessel transform.

Coupling structures of this type are of interest in multilayer millimeter-wave circuits, where the need for heat transfer from active devices often requires the use of relatively thick ground planes, as well as electrical interconnections between layers. Aperture coupling between layers is convenient since it eliminates the need for vias or other types of direct connections [1]–[4], which can be especially cumbersome when thick ground planes are involved. However, as shown in [5]–[7], coupling through a thick ground plane with an aperture that is below resonant size leads to an exponential decrease in coupling coefficient as ground-plane thickness increases, since the aperture appears as a waveguide section operating below cutoff. One approach to avoiding this problem is to use a coupling slot or aperture that is large enough to allow a propagating wave to pass through the thick ground plane, as in [8]. A more general approach is to form a resonant cavity in the ground plane between the substrate layers—this allows complete transmission and more design freedom. A similar idea was used to improve the coupling between a microstrip feed line and an aperture-coupled microstrip antenna having a thick ground plane [9].

It might be asked why custom-written computer codes and analysis are being developed for a problem of this type when commercially available electromagnetic CAD packages can model the same geometry. There are two reasons. First, the computational efficiency of a custom-written code is better than a general-purpose CAD package by at least an order of magnitude. For complicated geometries, such as this one, where many parameters may have to be optimized to achieve a working design, this can be critical. Secondly, a dedicated analysis of a problem like this one can lead to equivalent circuits based on physical parameters of the geometry, providing useful tools for design and optimization. Such equivalent circuits are not obtainable from general-purpose electromagnetic analysis packages.

II. Analysis of Cavity-oupled Microstrip Lines

A. Geometry of the Problem

The geometry of the cavity-coupled microstrip lines is shown in Fig. 1(a) and (b). For convenience, we label the bottom substrate as the feed-line substrate, and the top substrate as the coupled-line substrate. The feed substrate contains the feed microstrip line and the feed side-coupling slot. The coupled-line substrate contains the coupled microstrip line and the coupled side-coupling slot. The cavity is located between the ground planes of the two substrates, and may be filled with a dielectric material. The cavity may be rectangular or circular, and does not have to be resonant. We assume the microstrip lines are orthogonal to, and centered across the width of, the coupling slots, and that the coupling slots are centered with respect to the cavity endwalls. These conditions result in maximum coupling and simplify the analysis. Loss can be included for all three dielectric materials.

The structure shown in Fig. 1(a) and (b) involves four terminal ports (at the two ends of each microstrip line). A two-port

Manuscript received August 26, 2002; revised October 24, 2002. This work was supported by the Raytheon Company.

The author is with the Electrical and Computer Engineering Department, University of Massachusetts at Amherst, Amherst, MA 01003 USA.

Digital Object Identifier 10.1109/TMTT.2003.808702

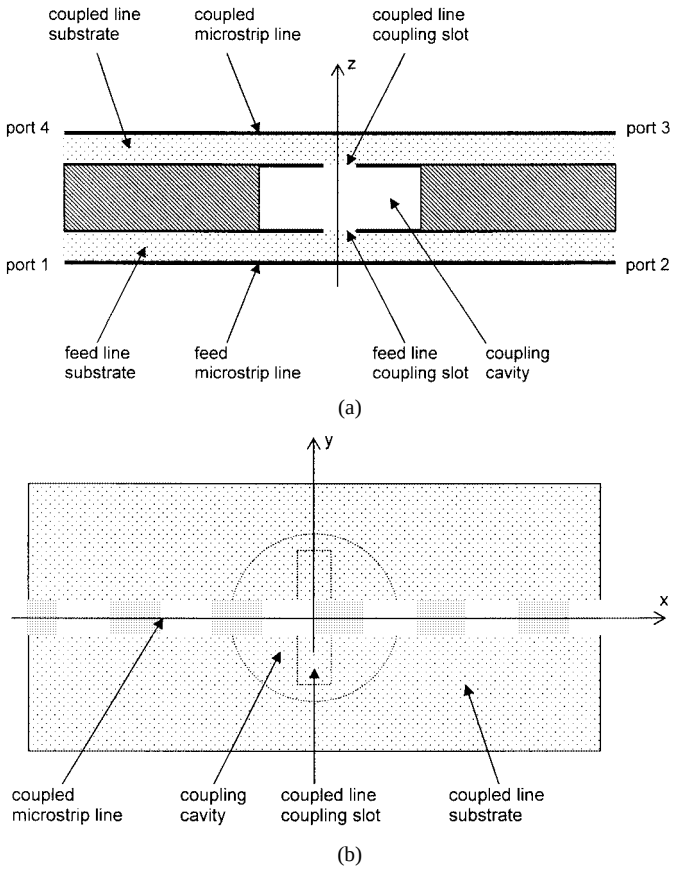

Fig. 1. (a) Side view of cavity coupled microstrip lines. (b) Top view of microstrip lines coupled with a circular cavity.

transition between the two layers can be easily formed by terminating each microstrip line with an open-circuit stub so that there is an input port on the feed line and an output port on the coupled line. The length of the stubs are design variables that must be selected, along with the slot and cavity dimensions, for the desired coupling level and input matching. Details of this procedure will be discussed.

B. Definition of Variables

The following parameters and variables are used in this paper.

ε_{rf}	Relative permittivity of the coupled-line substrate.
$\tan\delta_f$	Loss tangent of feed-line substrate.
d_f	Feed-line substrate thickness (m).
w_f	Width of feed microstrip line (m).
L_f	Length of feed side aperture (y-dimension m).
W_f	Width of feed side aperture (x-dimension m).
ε_{rc}	Relative permittivity of the feed-line substrate.
$\tan\delta_c$	Loss tangent of coupled-line substrate.
d_c	Coupled-line substrate thickness (m).
w_c	Width of coupled microstrip line (m).
L_c	Length of coupled side aperture (y-dimension m).
W_c	Width of coupled side aperture (x-dimension m).
a	x-dimension of rectangular cavity, radius of circular cavity (m).
b	y-dimension of rectangular cavity (m).
t	Thickness of cavity (ground-plane thickness (m).
$\varepsilon_{\rm rcav}$	Relative permittivity of cavity.
k_0	Free-space wavenumber $(1/m)$.

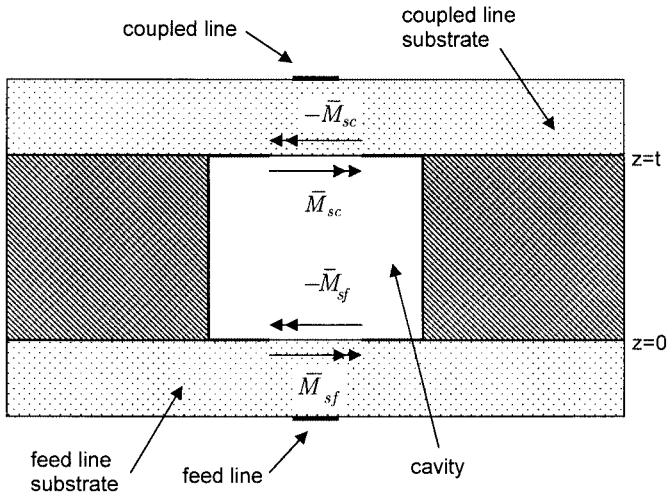

Fig. 2. Geometry of cavity-coupled microstrip lines showing the equivalent magnetic currents.

C. Moment-Method Analysis

The analysis begins by using the equivalence theorem to replace the slot apertures with ground planes, and placing equal, but opposite magnetic surface currents over the aperture areas. Fig. 2 shows the arrangement of the equivalent magnetic surface currents.

The magnetic surface currents in the apertures are assumed to flow only in the $\hat{y}$-direction, which is a good approximation for thin slots (but may be inaccurate if the slot is not thin). We can then express the magnetic surface current densities in the coupling apertures as

$$\bar{M}_{sf} = V_f m_y^f(x,y)\hat{y} \tag{1}$$

$$\bar{M}_{sc} = V_c m_y^c(x,y)\hat{y} \tag{2}$$

where V_f and V_c are the unknown amplitudes of the magnetic surface current expansions in the feed- and coupled-line apertures, respectively, and $m_y^{f,c}(x,y)$ is the expansion mode, where the superscript f, c denotes the feed or coupled slot mode. Since the slot length is generally below resonant size, a single piecewise sinusoidal (PWS) expansion mode is sufficient [2], [3]. We use a PWS expansion along the slot length, with a uniform distribution along the width

$$m_y(x,y) = \frac{1}{W}\frac{\sin k_e\left(\dfrac{L}{2}-|y|\right)}{\sin\dfrac{k_e L}{2}}, \quad \text{for } |x| < \frac{W}{2};\quad |y| < \frac{L}{2} \tag{3}$$

where L is the slot length and W is the slot width. k_e is the effective wavenumber to be used in the PWS expansion—a good choice is the average value of the wavenumbers in the two adjacent dielectric materials, i.e.,

$$k_e = k_0\sqrt{\frac{\varepsilon_{rf,c}+\varepsilon_{\rm rcav}}{2}}. \tag{4}$$

The fields on the feed microstrip line consist of incident and reflected waves to the left-hand side of the aperture, and a for-

ward transmitted wave to the right-hand side. These fields can be written as

$$\bar{E}(x,y,z) = \begin{cases} \bar{E}^+ + R\bar{E}^- = \left(e^{-j\beta x} + \mathrm{Re}^{j\beta x}\right)\bar{e}^f(y,z), & \text{for } x<0 \\ T\bar{E}^+ = T\bar{e}^f(y,z)e^{-j\beta x}, & \text{for } x>0 \end{cases} \tag{5}$$

$$\bar{H}(x,y,z) = \begin{cases} \bar{H}^+ + R\bar{H}^- = \left(e^{-j\beta x} - \mathrm{Re}^{j\beta x}\right)\bar{h}^f(y,z), & \text{for } x<0 \\ T\bar{H}^+ = T\bar{h}^f(y,z)e^{-j\beta x}, & \text{for } x>0. \end{cases} \tag{6}$$

The fields on the coupled line consist of waves traveling outward from the slot and can be written as

$$\bar{E}(x,y,z) = \begin{cases} C\bar{E}^+ = C\bar{e}^c(y,z)e^{-j\beta x}, & \text{for } x>0 \\ C\bar{E}^- = -C\bar{e}^c(y,z)e^{j\beta x}, & \text{for } x<0 \end{cases} \tag{7}$$

$$\bar{H}(x,y,z) = \begin{cases} C\bar{H}^+ = C\bar{h}^c(y,z)e^{-j\beta x}, & \text{for } x>0 \\ C\bar{H}^- = C\bar{h}^c(y,z)e^{j\beta x}, & \text{for } x<0. \end{cases} \tag{8}$$

In (5)–(8), we assume a unit incident field on the feed line at port 1 ($x<0$) and assume the output ports are matched. The following coefficients are then defined:

- R reflection coefficient on feed line at port 1;
- T transmission coefficient on coupled line at port 3;
- C coupling coefficient on coupled line at port 3.

The phase reference for all traveling waves is at the center of the aperture. We also define $\bar{e}(y,z)$ and $\bar{h}(y,z)$ as the transverse modal fields of the microstrip lines and use a superscript f or c to denote the feed or coupled line, respectively. The microstrip line modal fields are normalized so that

$$\int_S \bar{e}(y,z)\times\bar{h}(y,z)\cdot d\bar{S} = 1 \tag{9}$$

where S represents the cross section of the microstrip line. The modal fields of the microstrip line can be found using the appropriate Green's functions [2]. The propagation constant for the microstrip line is β, which may be different for the two lines.

The reciprocity method of [2] and [3] can be used to find the reflected, transmitted, and coupling coefficients in terms of the slot modal voltages

$$R = \frac{-\Delta v_f V_f}{2} \tag{10}$$

$$T = 1 - R \tag{11}$$

$$C = \frac{\Delta v_c V_c}{2}. \tag{12}$$

In (10) and (12), we are using the modal voltages defined as

$$\Delta v_f = -\int_{S_A} m_y(x,y)h_y^f(y,0)e^{-j\beta x}dS \tag{13}$$

$$\Delta v_c = -\int_{S_A} m_y(x,y)h_y^c(y,0)e^{-j\beta x}dS \tag{14}$$

where the integration is over the aperture surface and $h_y(x,y)$ is the y-component of the transverse modal field of either the feed or coupled microstrip line. These integrals must be determined numerically, but convergence is fairly fast.

Enforcing continuity of H_y across both sides of the feed aperture gives the following equation:

$$H_y^{\mathrm{cav}}\left(-\bar{M}_{sf}\right) + H_y^{\mathrm{cav}}(\bar{M}_{sc}) = H_y^f(\bar{M}_{sf}) + H_y^{fl} \tag{15}$$

where the notation $H_y^{\mathrm{cav},f}(\bar{M}_{sf,sc})$ refers to the magnetic field on the cavity or the feed-line side of the feed aperture, due to the magnetic surface current in the feed- or coupled-line aperture. The terms on the left-hand side of (15) represent the fields on the cavity side of the feed aperture due to the magnetic surface currents in the feed and coupled apertures, respectively. The terms on the right-hand side represent the fields on the feed substrate side of the aperture due to the magnetic surface current in the feed aperture, and the field from the microstrip feed line. Using (1), (2), and (6) in (15) gives

$$-V_f H_y^{\mathrm{cav}}\left(-m_y^f\right) + V_c H_y^{\mathrm{cav}}\left(m_y^c\right) = V_f H_y^f\left(m_y^f\right) + (1-R)h_y^f. \tag{16}$$

Applying a similar procedure for the continuity of H_y across the coupled side aperture gives

$$H_y^{\mathrm{cav}}\left(-\bar{M}_{sc}\right) + H_y^{cl} = H_y^{\mathrm{cav}}\left(\bar{M}_{sc}\right) + H_y^{\mathrm{cav}}\left(-\bar{M}_{sf}\right) \tag{17}$$

where the notation $H_y^{\mathrm{cav},c}(\bar{M}_{sf,sc})$ refers to the magnetic field on the cavity or coupled-line side of the coupled aperture due to the magnetic surface current in the feed- or coupled-line aperture. The terms on the left-hand side of (17) represent the fields on the coupled-line side of the aperture due to the magnetic surface current in the aperture, and the field from the coupled microstrip line. The terms on the right-hand side represent the fields on the cavity side of the aperture due to the magnetic surface currents in the coupled side aperture, and the feed side aperture, respectively. Using (1), (2), and (8) in (17) gives

$$-V_c H_y^{\mathrm{cav}}\left(m_y^c\right) + Ch_y^c = V_c H_y^{\mathrm{cav}}\left(m_y^c\right) - V_f H_y^{\mathrm{cav}}\left(m_y^f\right). \tag{18}$$

The above fields are expressible in terms of the appropriate Green's functions for the cavity (internal) or substrate (external) regions.

Multiplying both sides of (16) by the magnetic surface current expansion mode $m_y^f(x,y)$ and integrating over the feed aperture surface gives

$$V_f Y_{\mathrm{cav}}^{ff} - V_c Y_{\mathrm{cav}}^{fc} = -V_f Y_{\mathrm{ext}}^{ff} - (1-R)\,\Delta v_f \tag{19}$$

while multiplying both sides of (18) by the magnetic surface current expansion mode $m_y^c(x,y)$ and integrating over the coupled aperture surface gives

$$V_c Y_{\mathrm{cav}}^{cc} - C\Delta v_c = -V_c Y_{\mathrm{ext}}^{cc} + V_f Y_{\mathrm{cav}}^{cf}. \tag{20}$$

In (19) and (20), Y_{ext}^{ff} and Y_{ext}^{cc} are the aperture self-admittances seen looking outward from either the feed or coupled slot, respectively,

$$\begin{aligned} Y_{\mathrm{ext}}^{ff,cc} &= -\int_{S_A} m_y(x,y)h_y^f(y,0)e^{-j\beta x}dS \\ &= -\int_{k_y=-\infty}^{\infty}\int_{k_{x=-\infty}}^{\infty}\int_{S_A} m_y(x,y) \\ &\quad\times\int_{S_A} G_{H_yM_y}^{\mathrm{ext}}(k_x,k_y)m_y(x_0,y_0) \\ &\quad\times e^{-jk_x(x-x_0)}e^{-jk_y(y-y_0)}dSdS'dk_xdk_y. \end{aligned} \tag{21}$$

The following admittances represent internal coupling between the coupled and feed slots:

$$Y_{\text{cav}}^{ff} = -\int_{S_f}\int_{S_f} m_f(x,y) G_{H_y M_y}^{\text{cav}}(x,x_0;y,y_0;z=0) \times m_f(x_0,y_0)dx_0dy_0dxdy \quad (22)$$

$$Y_{\text{cav}}^{fc} = -\int_{S_f}\int_{S_f} m_f(x,y) G_{H_y M_y}^{\text{cav}}(x,x_0;y,y_0;z=t) \times m_c(x_0,y_0)dx_0dy_0dxdy \quad (23)$$

$$Y_{\text{cav}}^{cf} = -\int_{S_f}\int_{S_f} m_c(x,y) G_{H_y M_y}^{\text{cav}}(x,x_0;y,y_0;z=t) \times m_f(x_0,y_0)dx_0dy_0dxdy \quad (24)$$

$$Y_{\text{cav}}^{cc} = -\int_{S_f}\int_{S_f} m_c(x,y) G_{H_y M_y}^{\text{cav}}(x,x_0;y,y_0;z=0) \times m_c(x_0,y_0)dx_0dy_0dxdy. \quad (25)$$

The admittances defined in (22)–(25) represent the internal coupling between the magnetic currents on the top and bottom of the cavity. The self-admittances of the feed and coupled side currents are expressed in (22) and (25), while the mutual interaction between the feed and coupled aperture currents are expressed in (23) and (24)—these two terms should be identical by reciprocity.

By using (10) and (12) in (19) and (20) to eliminate R and C, the unknown magnetic current amplitudes V_f and V_c can be obtained. The results can be simplified by defining the following constants:

$$C_1 = Y_{\text{cav}}^{ff} + Y_{\text{ext}}^{ff} + \frac{\Delta v_f^2}{2} \quad (26)$$

$$C_2 = -Y_{\text{cav}}^{fc} \quad (27)$$

$$C_3 = Y_{\text{cav}}^{cf} \quad (28)$$

$$C_4 = -Y_{\text{cav}}^{cc} - Y_{\text{ext}}^{cc} - \frac{\Delta v_c^2}{2}. \quad (29)$$

We then have that

$$V_f = \frac{-\Delta v_f C_4}{C_1C_4 - C_2C_3} \quad (30)$$

$$V_c = \frac{\Delta v_f C_3}{C_1C_4 - C_2C_3}. \quad (31)$$

Once these amplitudes are determined, (10)–(12) can be used to find R, T, and C.

The substrate Green's function required for (13), (14), and (21) is given in [2] and [3]. The Green's functions for rectangular and circular cavities required for (22)–(25) are given in the Appendix. The Fourier transform integrations in (21)–(25) can be evaluated in closed form for a rectangular cavity [9], but must be numerically evaluated in the case of a circular cavity. The Bessel functions that appear in the expressions of circular cavity Green's functions further increase computation time. Nevertheless, the computation time per point is typically 1–2 s for the rectangular cavity, and 10–15 s for the circular cavity [on an 800-MHz personal computer (PC)]. These times are typically one to two orders of magnitude faster than solutions obtained with commercially available CAD software packages.

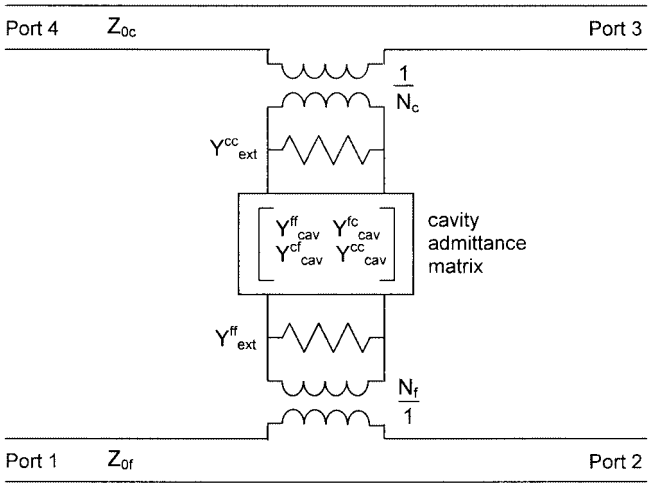

Fig. 3. Equivalent circuit of a cavity-coupled microstrip coupler. The cavity is represented in terms of its moment-method admittance matrix.

D. Equivalent Circuits

The equivalent circuit of the cavity-coupled microstrip-line coupler is similar to the equivalent circuit of aperture-coupled microstrip lines given in [3], with the addition of the cavity admittance matrix between the coupling transformers, as shown in Fig. 3. The admittance matrix of the slot-coupled cavity is given by the moment-method admittances of (22)–(25). The transformers account for the difference in definitions of transmission-line voltages and slot voltages, while the shunt admittances Y_{ext}^{cc} and Y_{ext}^{ff} represent the self-susceptances of the slots.

The transformer turns ratios are given by

$$N_f = \frac{1}{\Delta v_f \sqrt{Z_{0f}}} \quad (32)$$

$$N_c = \frac{1}{\Delta \nu_c \sqrt{Z_{0c}}}. \quad (33)$$

This is a fairly general representation of the coupler, but a more physical picture can be obtained if the cavity allows only a single propagating mode (in practice, the typical situation). The coupling from the feed-line slot to the coupled-line slot can then be represented as a section of transmission line, with transformers at each end to account for the transition between the slot voltages and equivalent modal voltage that can be defined for the waveguide [9], [10]. The resulting equivalent circuit is shown in Fig. 4, and is similar to the one used in [9] for cavity-coupled microstrip antennas.

In this circuit, the slot self-admittances of the cavity must be modified by subtracting the terms that account for propagation of power through the propagating waveguide mode (TE_{01} for rectangular waveguide or TE_{11} for circular waveguide). Thus,

$$Y_{\text{cav}}^{\prime ff} = Y_{\text{cav}}^{ff} - Y_{\text{prop}}^{ff} \quad (34)$$

$$Y_{\text{cav}}^{\prime cc} = Y_{\text{cav}}^{cc} - Y_{\text{prop}}^{cc} \quad (35)$$

where Y_{prop}^{ff} and Y_{prop}^{cc} represent the internal feed and coupled slot self-admittances due to only the propagating term of the cavity expansion. These admittances correspond to a single term of the series representation of the cavity Green's function. In the absence of losses, the modified admittances of (34) and (35)

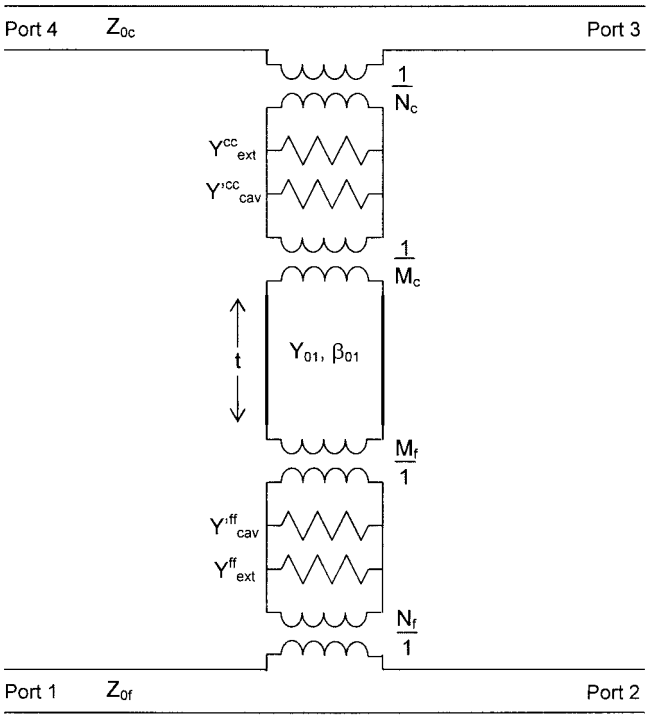

Fig. 4. Equivalent circuit of the cavity-coupled microstrip coupler. The cavity is represented as a section of transmission line.

would be purely imaginary, and account for the reactive effects of nonpropagating modes.

The transformer turns ratios for the additional transformers in Fig. 4 are defined in the Appendix for rectangular and circular cavities.

III. Two-Port Cavity-Coupled Microstrip Transition

Terminating each microstrip line with an open-circuited stub converts the four-port coupler to a two-port transition between the substrate layers. The equivalent circuit for this configuration is shown in Fig. 5, and is derived from the circuit of Fig. 4 by terminating ports 2 and 4 with reactances jX_{sf} and jX_{sc}, respectively, representing the reactances of the open-circuit stubs on the feed and coupled lines.

In this circuit, we have also combined the pairs of transformers on either side of the cavity, and transformed the admittances through these transformers. These new admittances are given as

$$Y'^{f} = N_f^2 \left(Y'^{ff}_{\text{cav}} + Y^{ff}_{\text{ext}} \right) \tag{36}$$

$$Y'^{c} = N_c^2 \left(Y'^{cc}_{\text{cav}} + Y^{cc}_{\text{ext}} \right). \tag{37}$$

Total coupling will occur between ports 1 and 3 if the input impedance of the transition is matched to Z_{0f}. There are a large number of interdependent parameters, however, that must be properly selected before such a design is possible. Besides the substrate parameters, these include the dimensions of both slots, the cross-sectional dimensions of the cavity, the length of the cavity, and the dielectric constant of the material filling the cavity. If these parameters allow a matched solution, the tuning

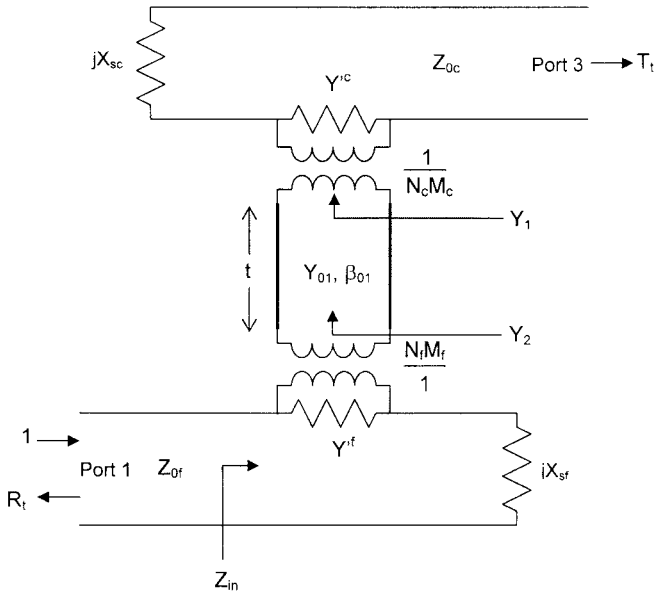

Fig. 5. Equivalent circuit of a two-port cavity-coupled microstrip transition.

stubs on ports 2 and 4 can be adjusted to provide a matched input.

If port 3 is terminated in a matched load of Z_{0c}, then the load admittance seen looking into the primary side of the coupled-line transformer of Fig. 5 can be expressed as

$$Y_1 = \frac{1}{N_c^2 M_c^2} \left(Y'^{c} + \frac{1}{Z_{0_c} + jX_{sc}} \right). \tag{38}$$

This admittance is then transformed through the transmission-line section

$$Y_2 = Y_{01} \frac{Y_1 + jY_{01} \tan \beta_{01} t}{Y_{01} + jY_1 \tan \beta_{01} t}. \tag{39}$$

Finally, the input impedance seen looking into port 1 is

$$Z_{in} = jX_{sf} + \frac{1}{Y'^{f} + N_f M_f Y_2}. \tag{40}$$

We can attempt a transition design by first choosing the coupled-line stub reactance jX_{sc} to cancel the reactance of Y'^{c}. Using (37) then leads to the following formula for X_{sc}:

$$\frac{X_{sc}}{Z_{0c}} = \frac{-1 \pm \sqrt{1 - 4A^2}}{2A} \tag{41}$$

where $A = -N_c^2 Z_{0c} \text{Im} \{ Y'^{cc}_{\text{cav}} + Y^{cc}_{\text{ext}} \}$. If the argument of the square-root term in (41) is negative, then no matching solution is possible—this usually means that the slot length is too small or that the cavity parameters do not allow a propagating mode. Once the reactance is found from (41), the coupled-line stub length ℓ_{sc} can be found from

$$jX_{sc} = -jZ_{0c} \cot \beta \ell_{sc}. \tag{42}$$

The input impedance can then be made real by using the feed-line stub to cancel the reactance of Y_2, which yields the following equation for X_{sf}:

$$X_{sf} = -\text{Im} \left\{ \frac{1}{Y'^{f} + N_f M_f Y_2} \right\}. \tag{43}$$

The above procedure only yields a real input impedance—the real part of the input impedance must still be matched to Z_{0f} by proper selection of the slot and cavity parameters. This can be very difficult in practice.

The design procedure outlined above generally results in a transition with different stub lengths for the feed and coupled lines, even if the two substrates are identical. From symmetry, it is clear that a design where both stub lengths are the same must be possible, but we have not been able to derive a simple closed-form solution (in terms of the equivalent-circuit parameters) for this case. Finally, note that it is also possible to terminate port 3 with an open-circuited stub, with port 4 used as the output port. This will lead to the same results as above, except for a 180° phase shift in the output voltage. It is also possible to obtain a broad-band 180° 3-dB splitter by using both ports 3 and 4 as output ports.

A. Transition Response

The response of the two-port transition can be found using the equivalent circuit of Fig. 5 [after the parameters of this circuit have been found from the moment-method analysis and (25)–(27)], but a more direct method is to convert the S-parameters of the four-port coupler to the S parameters of the two-port transition. Due to symmetry, there are only four unique parameters in the 4×4 S matrix of the coupler (one row or column). These can be written in terms of the R, T, and C parameters defined above in the moment-method analysis as

$$S_{11} = R = \frac{-\Delta v_f V_0}{2} \tag{44}$$

$$S_{12} = 1 - S_{11} = T = 1 - R \tag{45}$$

$$S_{13} = C = \frac{\Delta v_c V_0}{2} \tag{46}$$

$$S_{14} = -S_{13} = -C = \frac{-\Delta v_c V_0}{2}. \tag{47}$$

Fig. 6 shows a block diagram of a four-port coupler with ports 2 and 4 terminated with loads having reflection coefficients Γ_{sf} and Γ_{sc}, respectively. These coefficients are determined from the stub reactances jX_{sf} and jX_{sc}

In Fig. 6, we assume a unit amplitude wave incident at port 1, and refer to the reflection coefficient at port 1 as R_t, and the transmission coefficient at port 3 as T_t, to distinguish these coefficients from the corresponding terms R and T defined for the four-port coupler of Fig. 3. A straightforward, but lengthy analysis gives R_t and T_t in terms of the four-port S-parameters as follows:

$$R_t = S_{11} + \frac{S_{14}^2 \Gamma_{sc}}{1 - S_{44}\Gamma_{sc}} + \left(S_{12} + \frac{S_{14} S_{24} \Gamma_{sc}}{1 - S_{44}\Gamma_{sc}} \right) \times \frac{S_{21}\Gamma_{sf}(1 - S_{44}\Gamma_{sc}) + S_{14} S_{24} \Gamma_{sc} \Gamma_{sf}}{(1 - S_{22}\Gamma_{sf})(1 - S_{44}\Gamma_{sc}) - S_{24}^2 \Gamma_{sc} \Gamma_{sf}} \tag{48}$$

$$T_t = S_{31} + \frac{S_{14} S_{34} \Gamma_{sc}}{1 - S_{44}\Gamma_{sc}} + \left(S_{32} + \frac{S_{24} S_{34} \Gamma_{sc}}{1 - S_{44}\Gamma_{sc}} \right) \times \frac{S_{21}\Gamma_{sf}(1 - S_{44}\Gamma_{sc}) + S_{14} S_{24} \Gamma_{sc} \Gamma_{sf}}{(1 - S_{22}\Gamma_{sf})(1 - S_{44}\Gamma_{sc}) - S_{24}^2 \Gamma_{sc} \Gamma_{sf}}. \tag{49}$$

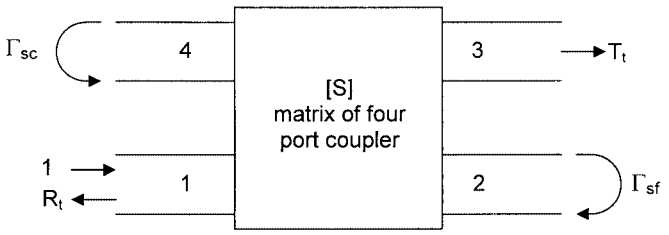

Fig. 6. Block diagram of the four-port coupler terminated with loads to form a two-port transition.

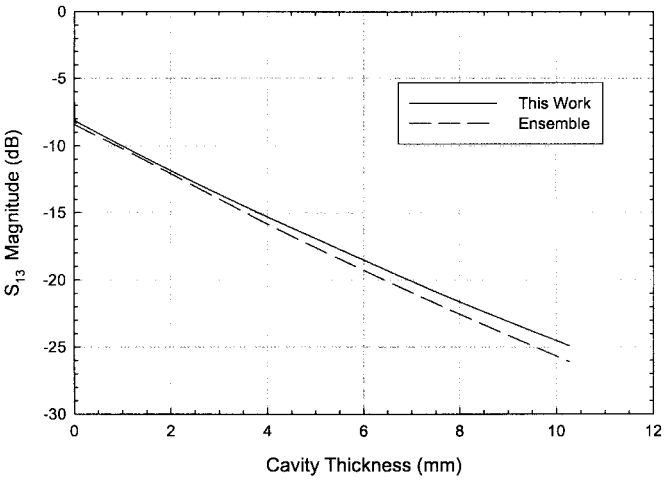

Fig. 7. Calculated coupling of a four-port coupler with a thick ground plane (rectangular cavity) compared with data from *Ensemble*. $f = 4$ GHz, $\varepsilon_{rf} = \varepsilon_{rc} = 2.22$, $d_f = d_c = 0.0762$ cm, $\tan\delta_f = \tan\delta_c = 0.001$, $b = L_f = L_c = 1.5$ cm, $a = W_f = W_c = 0.11$ cm, $t = 0 - 1.026$ cm, $\varepsilon_{\text{rcav}} t = 2.22$, and $w_f = w_c = 0.254$ cm.

IV. Examples

A. Rectangular Cavity

The solution described above was first validated by comparison with the zero-thickness ground-plane case described in [3]. We next considered coupling through a thick ground plane, which is the limiting case of a rectangular cavity having cross-sectional dimensions equal to the feed and coupling slot dimensions, i.e., $a = W_f = W_c$ and $b = L_f = L_c$. We attempted to compare with calculated data from [6], but noticed that the calculations presented in Fig. 2 of that paper are clearly in error, as they indicate an *increase* in coupling with an increase in ground-plane thickness, rather than a decrease (although the zero-thickness ground plane data of [6] did agree with our earlier published data given in [3]). Instead, we used a similar geometry as in [6], and compared our results with calculations from Ansoft's *Ensemble*, at a fixed frequency of 4 GHz, with ground-plane thickness ranging from 0 to 10.26 mm. Calculated results for $|S_{13}|$ are shown in Fig. 7 versus ground-plane (cavity) thickness at a frequency of 4 GHz. Note that coupling drops quickly with an increase in ground-plane thickness and that there is good agreement between our results and those from *Ensemble*. There is a slight difference between the two results that increases to approximately 1.5 dB for a ground-plane thickness of 10 mm—the reason for this disparity is not clear.

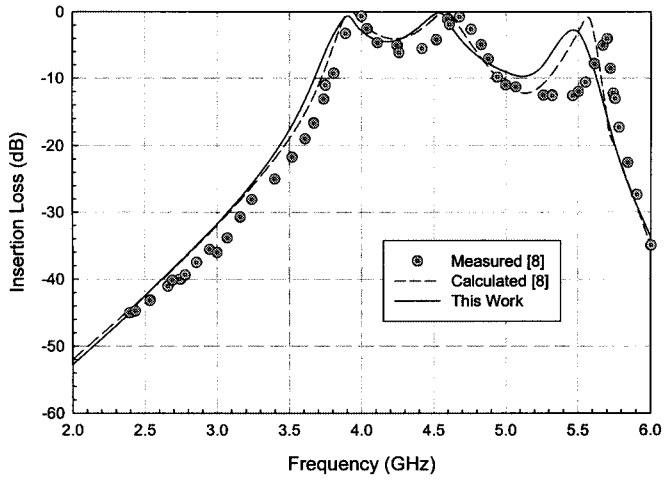

Fig. 8. Calculated insertion loss compared with calculations and measurements from [8] for a two-port microstrip transition with a thick ground plane (rectangular cavity). $\varepsilon_{rf} = \varepsilon_{rc} = 2.20$, $d_f = d_c = 0.158$ cm, $\tan\delta_f = \tan\delta_c = 0.001$, $b = L_f = L_c = 1.27$ cm, $a = W_f = W_c = 0.254$ cm, $t = 2.54$ cm, $\varepsilon_{\rm rcav} = 10.5 \pm 0.25$, $w_f = w_C = 0.498$ cm, and $\ell_{sf} = \ell_{sc} = 1.651$ cm.

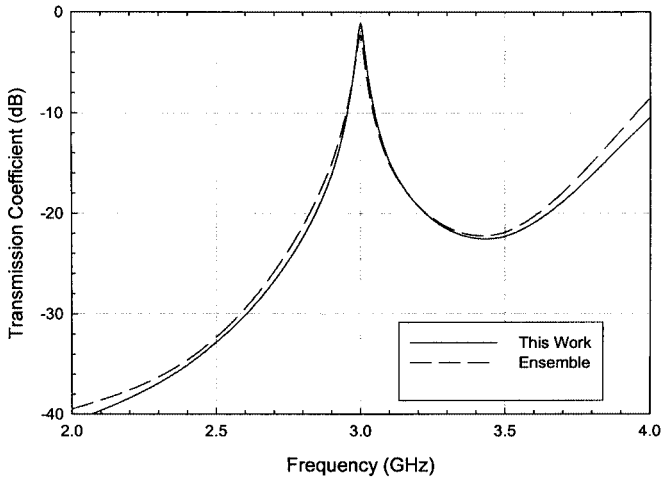

Fig. 9. Calculated insertion loss compared with results from *Ensemble* for a two-port microstrip transition with a large rectangular cavity. $\varepsilon_{rf} = \varepsilon_{rc} = 2.20$, $d_f = d_c = 0.0762$ cm, $\tan\delta_f = \tan\delta_c = 0.001$, $L_f = L_c = 2.70$ cm, $W_f = W_c = 0.11$ cm, $a = b = 4.04$ cm, $t = 6.12$ cm, $\varepsilon_{\rm rcav} = 2.20$, $w_f = w_c = 0.254$ cm, $\ell_{sf} = 1.710$ cm, and $\ell_{sc} = 1.677$ cm.

For an independent calculation, we can model to a very good approximation the variation of coupling with ground-plane thickness by assuming a single evanescent mode in the waveguide; i.e., for a reasonably thick ground plane, the coupling must vary as

$$|S_{13}| = Ae^{-\alpha t} \tag{50}$$

where A is the coupling level for $t = 0$ and α is the attenuation constant of the evanescent waveguide mode

$$\alpha = \sqrt{\left(\frac{\pi}{b}\right)^2 - \varepsilon_{\rm rcav} k_0^2}. \tag{51}$$

At $t = 0$, the coupling level is -8.1 dB, and we can calculate $\alpha = 168.2$ m^{-1} from (51). For $t = 10.26$ mm, (50) gives $|S_{13}| = -23.1$ dB, which is within approximately 1 dB of our calculated results.

Next, we compared our calculations with the measurements and calculations for the two-port microstrip transition with a thick ground plane presented in [8]. Note that this is a symmetric transition, having the same substrates and stub lengths on both the feed- and coupled-line sides of the structure. Also note that the cavity has a filling with a high dielectric constant with a relatively large tolerance. Results for insertion loss versus frequency are shown in Fig. 8. Agreement appears to be very good, and the highly resonant behavior is modeled quite well. There is a slight shift between measured and calculated results for the resonant peak at the highest frequency, but this may be attributable to the uncertainty in the dielectric constant of the material filling the cavity. Small air gaps in the physical model may have a similar effect on the measured data. The cutoff frequency of the connecting waveguide is approximately 3.64 GHz—the data clearly show that below this frequency strong coupling is not possible.

For a third example, we treat a two-port coupler with a rectangular cavity having a size different than the coupling slots. Note that the ground plane thickness is 6.12 cm—this dimension is $\lambda_g/2$ in the dielectric-filled waveguide at 3 GHz. The calculated insertion loss for this transition is plotted versus frequency in Fig. 9 and compared with results from *Ensemble*. Agreement is quite good, and the high-Q nature of coupling with the cavity can be clearly seen. We also compared the S-parameters for the four-port version of this geometry with *Ensemble* with good agreement for both magnitude and phase.

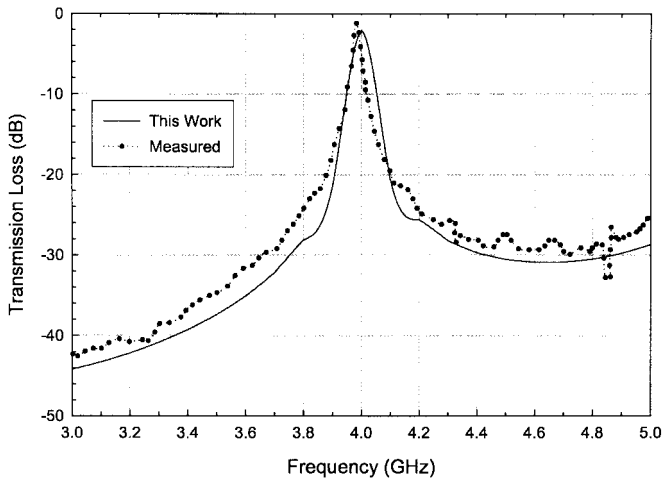

Fig. 10. Comparison of measured and calculated insertion loss for a two-port transition using a circular cavity. $\varepsilon_{rf} = \varepsilon_{rc} = 2.20$, $d_f = d_c = 0.0787$ cm, $\tan\delta_f = \tan\delta_c = 0.001$, $L_f = L_c = 2.40$ cm, $W_f = W_c = 0.2$ cm, $a = 2.64$ cm, $t = 6.77$ cm, $\varepsilon_{\rm rcav} = 1.0$, $w_f = w_c = 0.242$ cm, and $\ell_{sf} = \ell_{sc} = 1.26$ cm.

B. Circular Cavity

There are no results for microstrip couplers using circular cavities in the literature and *Ensemble* does not treat circular cavities, thus, a microstrip transition using a circular cavity was fabricated and tested. The cavity was designed to have a resonant frequency of 4 GHz. The results are shown in Fig. 10, where it is seen that the present solution is in good agreement with measured data.

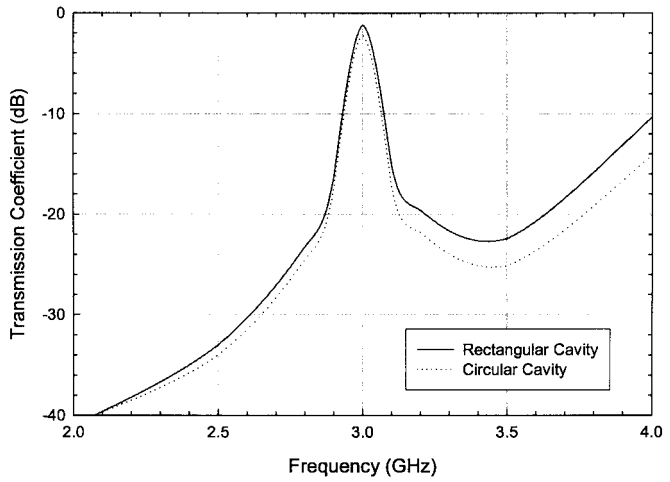

Fig. 11. Comparison of calculated insertion loss for two-port transitions using either a rectangular (square) cavity or a circular cavity. Both cavities have a resonant frequency of 3 GHz. $\varepsilon_{rf} = \varepsilon_{rc} = 2.20$, $d_f = d_c = 0.0762$ cm, $\tan\delta_f = \tan\delta_c = 0.001$, $L_f = L_c = 2.70$ cm, $W_f = W_c = 0.11$ cm, $a = b = 4.04$ cm (rectangular cavity), $a = 2.3705$ cm (circular cavity), $t = 6.12$ cm, $\varepsilon_{\rm rcav} = 2.20$, $w_f = w_c = 0.254$ cm, $\ell_{sf} = 1.710$ cm, and $\ell_{sc} = 1.677$ cm.

Another interesting comparison is to compare the response of a coupler using a circular cavity with that of a coupler using a square cavity having the same resonant frequency. The rectangular cavity transition treated in Fig. 9 was square in cross section, dielectric filled, $\lambda_g/2$ in length, and had a resonant frequency of 3 GHz. If we use a circular cavity of the same physical length with a radius chosen so that the resonant frequency is also 3 GHz, we should expect to see a similar response. Indeed, this is the case, as seen in the data of Fig. 11.

V. Conclusion

This paper has described a full-wave moment-method analysis of an aperture-coupled microstrip coupler using a resonant cavity between the substrate ground planes. Both four-port coupler geometries and two-port transitions have been treated. Equivalent circuits have been derived for each of these problems, and computed results have been validated with data from the literature and with independent calculations from commercial CAD packages and measured data. These comparisons have shown that the solutions derived here are accurate and computationally efficient, and have the added advantage over commercial CAD packages in that equivalent-circuit parameters can be obtained directly. The vector Bessel transform was used to derive the required Green's function for the circular cavity.

It was found that a cavity may be inserted between the substrate ground planes of two aperture-coupled microstrip lines, although the coupling level may decrease slightly (this can be compensated for by increasing the size of the coupling slots). In addition, the resonant nature of the cavity results in a much narrower bandwidth over which tight coupling can be achieved. Another possible disadvantage of introducing the cavity is that it appears that significant coupling only occurs when the cavity is resonant, meaning that the electrical length of the cavity (ground-plane thickness) must be $\lambda_g/2$—this may result in impractically thick ground planes unless the frequency is very high.

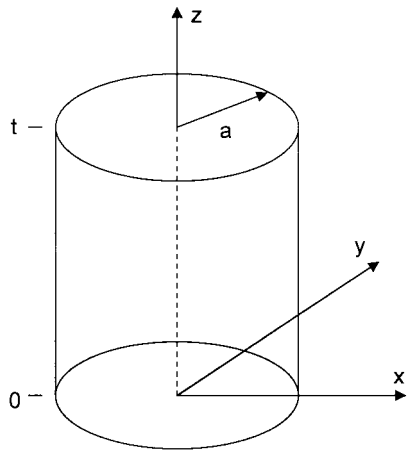

Fig. 12. Geometry of a circular cavity.

Appendix

Rectangular Cavity Green's Function

The required Green's function for the rectangular cavity gives the y component of the magnetic field at (x, y, z) due to a y-directed magnetic current at $(x_0, y_0, z_0 = 0)$. This result can be used to evaluate both self-admittance and mutual admittance between two slots located in the endwalls of the cavity by setting $z = 0$ for self-admittances and $z = t$ for mutual admittances. The cross section of the cavity is assumed to extend from $0 < x < a$ and $0 < y < b$ and from $0 < z < t$ in height as follows:

$$H_y = \frac{2j}{k_0\eta_0 ab}\sum_{m=0}^{\infty}\sum_{n=1}^{\infty}\frac{\varepsilon_{0m}\left[\varepsilon_r k_0^2 - k_y^2\right]}{k_z \sin k_z t} \times \cos k_x x \cos k_x x_0 \sin k_y y \sin k_y y_0 \cos k_z(t-z). \tag{A.1}$$

In this expression, the following variables are defined:

$$k_x = \frac{m\pi}{a} \tag{A.2}$$

$$k_y = \frac{n\pi}{b} \tag{A.3}$$

$$k_z = \sqrt{\varepsilon_r k_0^2 - k_x^2 - k_y^2}, \qquad \mathrm{Im}\{k_z\} < 0 \tag{A.4}$$

$$\varepsilon_{0m} = \begin{cases} 1, & \text{for } m = 0 \\ 2, & \text{for } m \neq 0. \end{cases} \tag{A.5}$$

For a rectangular slot centered in the cavity endwall, terms in the series with m odd or n even are zero. Note that (A.1) is a space-domain (not spectral-domain) representation.

Derivation of Circular-Cavity Green's Function

The circular-cavity Green's function for vector magnetic current sources has not, to our knowledge, appeared in the literature and, therefore, its derivation is outlined here using the Fourier–Bessel transform technique described in [12]. The geometry of the circular cavity is shown in Fig. 12. The radius is

a, the height is t, and the material filling the cavity has a relative dielectric constant of ε_r.

A magnetic current on one of the cavity endwalls will excite both TE and TM modes in the cavity. Thus, the fields can be expressed in terms of the electric and magnetic vector potentials as [11]

$$E_\rho = \frac{-j}{\omega\mu\varepsilon}\frac{\partial^2 A_z}{\partial\rho\partial z} - \frac{1}{\varepsilon\rho}\frac{\partial F_z}{\partial\phi} \tag{A.6}$$

$$E_\phi = \frac{-j}{\omega\mu\varepsilon\rho}\frac{\partial^2 A_z}{\partial\phi\partial z} - \frac{1}{\varepsilon}\frac{\partial F_z}{\partial\rho} \tag{A.7}$$

$$E_z = \frac{-j}{\omega\mu\varepsilon}\left(k^2 + \frac{\partial^2}{\partial z^2}\right)A_z \tag{A.8}$$

$$H_\rho = \frac{1}{\mu\rho}\frac{\partial A_z}{\partial\phi} - \frac{j}{\omega\mu\varepsilon}\frac{\partial^2 F_z}{\partial\rho\partial z} \tag{A.9}$$

$$H_\phi = \frac{-1}{\mu}\frac{\partial A_z}{\partial\rho} - \frac{-j}{\omega\mu\varepsilon\rho}\frac{\partial^2 F_z}{\partial\phi\partial z} \tag{A.10}$$

$$H_z = \frac{-j}{\omega\mu\varepsilon}\left(k^2\frac{\partial^2 F_z}{\partial z^2}\right)F_z. \tag{A.11}$$

The vector potentials can be expressed in Fourier–Bessel series form as

$$A_z = \sum_{n=-\infty}^{\infty}\sum_{m=1}^{\infty} A_{nm}^{\pm} J_n(k_{nm}\rho)e^{jn\phi} \times \begin{cases}\cos k_z(t-z), & z > z'\\ \cos k_z z, & z < z'\end{cases} \tag{A.12}$$

$$F_z = \sum_{n=-\infty}^{\infty}\sum_{m=1}^{\infty} F_{nm}^{\pm} J_n(k'_{nm}\rho)\, e^{jn\phi} \times \begin{cases}\sin k'_z(t-z), & z > z'\\ \sin k'_z z, & z < z'\end{cases} \tag{A.13}$$

where the following terms are defined:

$$k_{nm} = \frac{x_{nm}}{a}$$
$$J_n(x_{nm}) = 0 \tag{A.14}$$
$$k'_{nm} = \frac{x'_{nm}}{a}$$
$$J'_n(x'_{nm}) = 0 \tag{A.15}$$
$$k_z^2 = \varepsilon_r k_0^2 - k_{nm}^2 \tag{A.16}$$
$$k_z'^2 = \varepsilon_r k_0^2 - k'^2_{nm}. \tag{A.17}$$

Note that the radial and z-dependencies of the potentials have been chosen to satisfy the boundary conditions that $E_\rho = 0$ and $E_\phi = 0$ at $z = 0$ and $z = t$, and that $E_\phi = 0$ at $\rho = a$.

Next we define the vector Bessel transform pair as [12]

$$\bar{f}_n(\rho) = \sum_{m=1}^{\infty}\overline{\overline{J}}_{nm}(\rho)\cdot\bar{F}_{nm} \tag{A.18}$$

$$\bar{F}_{nm} = \overline{\overline{C}}_{nm}^{-1}\int_{\rho=0}^{a}\overline{\overline{J}}_{nm}^{t}(\rho)\cdot\bar{f}_n(\rho)\rho d\rho \tag{A.19}$$

where the following matrices are defined:

$$\overline{\overline{J}}_{nm}(\rho) = \begin{bmatrix} J'_n(k_{nm}\rho) & \dfrac{-jn}{k'_{nm}\rho}J_n(k'_{nm}\rho)\\ \dfrac{jn}{k_{nm}\rho}J_n(k_{nm}\rho) & J'_n(k'_{nm}\rho)\end{bmatrix} \tag{20}$$

$$\overline{\overline{C}}_{nm} = \begin{bmatrix}\dfrac{a^2}{2}J_{n+1}(k_{nm}a) & 0\\ 0 & \dfrac{a^2}{2}\left(1-\dfrac{n^2}{k'^2_{nm}a^2}\right)J_n^2(k'_{nm}a)\end{bmatrix}. \tag{A.21}$$

With these definitions, it can be shown that the following identity results from (A.18) and (A.19):

$$\int_{\rho=0}^{a}\overline{\overline{J}}_{nm}^{t}(\rho)\cdot\overline{\overline{J}}_{n\ell}(\rho)\rho d\rho = \overline{\overline{C}}_{nm}\delta_{m\ell} \tag{A.22}$$

where the superscript t represents transpose and $\delta_{m\ell}$ is the Kronecker delta symbol

$$\delta_{m\ell} = \begin{cases}1, & m = \ell\\ 0, & m \neq \ell.\end{cases}$$

The vector Bessel transform greatly simplifies the manipulation and inversion of the vector potentials and the associated coefficients. Thus, using (A.6) and (A.7), (A.12) and (A.13), and (A.20) allows the transverse electric field in the cavity to be expressed as

$$\begin{bmatrix}E_\rho\\ E_\phi\end{bmatrix} = \sum_{n=-\infty}^{\infty}\sum_{m=1}^{\infty}\overline{\overline{J}}_{nm}(\rho) \cdot\begin{bmatrix}\dfrac{-jA_{nm}^{+}k_z k_{nm}}{\omega\mu\varepsilon}\sin k_z(t-z)\\ \dfrac{k'_{nm}F_{nm}^{+}}{\varepsilon}\sin k'_z(t-z)\end{bmatrix}e^{jn\phi}. \tag{A.23}$$

The relation of (A.19) can then be used to invert (36) to find the unknown coefficients in terms of the transverse electric fields

$$\begin{bmatrix}\dfrac{-jA_{nm}^{+}k_z k_{nm}}{\omega\mu\varepsilon}\sin k_z(t-z)\\ \dfrac{k'_{nm}F_{nm}^{+}}{\varepsilon}\sin k'_z(t-z)\end{bmatrix} = \frac{1}{2\pi}\int_{\phi=0}^{2\pi}\int_{\rho=0}^{a}\overline{\overline{C}}_{nm}^{-1}\cdot\overline{\overline{J}}_{nm}^{t}(\rho)\cdot\begin{bmatrix}E_\rho\\ E_\phi\end{bmatrix}e^{-jn\phi}\rho d\rho\, d\phi. \tag{A.24}$$

Now assume a magnetic surface current source $\bar{M}_s = \hat{y}M_y$ on the bottom endwall at $z = 0$. Since $\bar{M}_s = \bar{E}\times\hat{n}$, we have that $E_\rho(\rho,\phi,0) = -M_\phi(\rho,\phi)$ and $E_\phi(\rho,\phi,0) = M_\rho(\rho,\phi)$ at

$z = 0$. Thus, (A.24) can be rewritten in terms of the cylindrical components of the source current as

$$\begin{bmatrix} \dfrac{-jA^+_{nm}k_z k_{nm}}{\omega\mu\varepsilon}\sin k_z t \\ \dfrac{k'_{nm}F^+_{nm}}{\varepsilon}\sin k'_z t \end{bmatrix} = \frac{1}{2\pi}\int_{\phi=0}^{2\pi}\int_{\rho=0}^{a} \overline{\overline{C}}^{-1}_{nm}\cdot\overline{\overline{J}}^{t}_{nm}(\rho)\cdot\begin{bmatrix} -M_\phi \\ M_\rho \end{bmatrix} e^{-jn\phi}\rho\, d\rho\, d\phi. \tag{A.25}$$

The cylindrical components of the source current are given in terms of the rectangular component as

$$M_\rho(\rho,\phi) = M_y(x,y)\sin\phi$$
$$M_\phi(\rho,\phi) = M_y(x,y)\cos\phi.$$

The required matrix product $\overline{\overline{C}}^{-1}_{nm}\cdot\overline{\overline{J}}^{t}_{nm}(\rho)$ can be found as (A.26), shown at the bottom of this page. The integration in (A.25) can be evaluated numerically to give A^+_{nm} and F^+_{nm}, i.e., the coefficients of the vector potentials for $z > 0$. This can be done most efficiently by calculating a two-dimensional array of coefficients for a finite range of n and m. The integration in (A.25) is over the magnetic surface current density; in this case, the slot on either the feed- or coupled-line substrate. This can be facilitated by converting the integration in (A.25) to rectangular coordinates.

After the A^+_{nm} and F^+_{nm} coefficients have been determined, the transverse magnetic fields can be computed as follows:

$$\begin{bmatrix} H_\phi \\ -H_\rho \end{bmatrix} = \sum_{n=-\infty}^{\infty}\sum_{m=1}^{\infty}\overline{\overline{J}}_{nm}(\rho)\cdot\begin{bmatrix} \dfrac{-k_{nm}A^+_{nm}}{\mu}\cos k_z(t-z) \\ \dfrac{-jk'_{nm}k'_z F^+_{nm}}{\omega\mu\varepsilon}\cos k'_z(t-z) \end{bmatrix} e^{jn\phi}. \tag{A.27}$$

The y-component of the magnetic field is found from (A.27) as $H_y = H_\rho\sin\phi + H_\phi\cos\phi$. These results can be used for all four terms of the cavity admittances, defined in (22)–(25), between the feed and coupled substrate slots by letting the source be located at $z = 0$, and the test source be located at either $z = 0$ (for the self-admittance terms) or $z = t$ (for the mutual admittance terms). We have found that the admittances converge fairly well with the series in (A.27) truncated for $-6 \le n \le 6$ and $1 \le m \le 6$, but more terms may be required for certain parameters. Also, due to symmetry for a centered coupling slot, the A^+_{nm} and F^+_{nm} coefficients computed from (A.25) are identically zero for n even.

Transformer Turns Ratio for Rectangular Cavity

For a propagating TE_{01} rectangular waveguide mode, the transformer turns ratios used in the equivalent circuit of Fig. 4 are given by [9]

$$M_f = \sqrt{\frac{2}{ab}}C_{yf} \tag{A.28}$$

$$M_c = \sqrt{\frac{2}{ab}}C_{yc} \tag{A.29}$$

where a and b are the dimensions of the waveguide cross section, and C_{yf} and C_{yc} are constants related to the modal voltages of the TE_{01} waveguide mode

$$C_{yf} = F_{m_f}\left(k_x = 0,\, k_y = \frac{\pi}{b}\right) \tag{A.30}$$

$$C_{yc} = F_{m_c}\left(k_x = 0,\, k_y = \frac{\pi}{b}\right). \tag{A.31}$$

Y_{01} and β_{01} are the wave admittance and propagation constant for the TE_{01} waveguide mode, and $F_{mf,c}$ is the Fourier transform of the PWS expansion mode used in the feed or coupled slot

$$F_m(k_x,k_y) = \frac{2k_e\left[\cos\dfrac{k_y L}{2} - \cos\dfrac{k_e L}{2}\right]}{\left(k_e^2 - k_y^2\right)\sin\dfrac{k_e L}{2}}\,\frac{\sin\dfrac{k_x W}{2}}{\dfrac{k_x W}{2}}. \tag{A.32}$$

Transformer Turns Ratios for Circular Cavity

The transformer turns ratios M_f and M_c for the circular cavity can be derived by first defining equivalent voltages for the dominant TE_{11} circular waveguide mode in terms of the waveguide modal fields [10]

$$\bar{E} = A^+\bar{e}e^{-j\beta z} = \frac{\bar{e}}{C_1}V^+e^{-j\beta z} \tag{A.33}$$

$$\bar{H} = A^+\bar{h}e^{-j\beta z} = \frac{\bar{h}}{C_2}\frac{V^+}{Z_{11}}e^{-j\beta z} \tag{A.34}$$

where $\bar{e}$ and $\bar{h}$ are the transverse modal fields of the TE_{11} mode, C_1 and C_2 are constants to be determined, V^+ is the voltage on the equivalent transmission line, and A^+ is the amplitude of the transverse waveguide fields. Also, $Z_{11} = \omega\mu/\beta$ is the wave impedance of the mode, and β is the propagation constant. Thus, we see that $V^+ = C_1A^+ = C_2Z_{11}A^+$.

For our purposes, we can define the transverse fields of the TE_{11} circular waveguide mode as

$$\bar{e} = \hat{\rho}\frac{2}{k_c\rho}J_1(k_c\rho)\cos\phi - \hat{\phi}2J'_1(k_c\rho)\sin\phi \tag{A.35}$$

$$\bar{h} = \hat{\rho}\frac{2}{Z_{11}}J'_1(k_c\rho)\sin\phi + \hat{\phi}\frac{2}{k_c\rho Z_{11}}J_1(k_c\rho)\cos\phi. \tag{A.36}$$

$$\overline{\overline{C}}^{-1}_{nm}\cdot\overline{\overline{J}}^{t}_{nm}(\rho) = \begin{bmatrix} \dfrac{2J'_n(k_{nm}\rho)}{a^2J^2_{n+1}(k_{nm}a)} & \dfrac{2jnJ_n(k_{nm}\rho)}{a^2k_{nm}\rho J^2_{n+1}(k_{nm}a)} \\ \dfrac{-2jnJ_n(k'_{nm}\rho)}{a^2k'_{nm}\rho\left(1-\frac{n^2}{k'^2_{nm}a^2}\right)J^2_n(k'_{nm}a)} & \dfrac{2J'_n(k'_{nm}\rho)}{a^2\left(1-\dfrac{n^2}{k'^2_{nm}a^2}\right)J^2_n(k'_{nm}a)} \end{bmatrix} \tag{A.26}$$

In these expressions, $k_c = x'_{nm}/a = 1.8412/a$ is the cutoff wavenumber of the TE_{11} mode.

The definition of equivalent voltages also requires normalization of power so that

$$\begin{aligned} P_0 &= \int_{\phi=0}^{2\pi}\int_{\rho=0}^{a} \bar{e}\times\bar{h}\cdot\hat{z}\rho d\rho d\phi \\ &= C_1 C_2 \\ &= \frac{2\pi}{Z_{11}}\left(x'^2_{11}-1\right)J_1^2\left(x'_{11}\right). \end{aligned} \tag{A.37}$$

Using (A.33), (A.34), and (A.37) gives expressions for the constants C_1 and C_2 in terms of the power in the waveguide mode and its wave impedance

$$C_1 = \sqrt{P_0 Z_{11}} \tag{A.38}$$

$$C_2 = \sqrt{\frac{P_0}{Z_{11}}}. \tag{A.39}$$

Now, by reciprocity, the excitation of the TE_{11} waveguide mode due to the magnetic current in the slot can be computed as [2], [10]

$$\begin{aligned} A^+ &= \frac{-1}{2P_0}\int \bar{h}\cdot 2\bar{M} \\ &= \frac{-V_0}{P_0}\int_{y=-L/2}^{L/2}\int_{x=-W/2}^{W/2}[h_\rho\sin\phi + h_\phi\cos\phi] \\ &\quad \times m_y(x,y)dxdy. \end{aligned} \tag{A.40}$$

This integration must be done numerically. Defining the integral as

$$C_y = \int_{y-L/2}^{L/2}\int_{x=-W/2}^{W/2}[h_\rho\sin\phi + h_\phi\cos\phi]\, m_y(x,y)dxdy$$

and using (A.38) and (A.40), allows the turns ratio to be calculated as

$$M = \frac{V^+}{V_0} = \frac{C_1 A^+}{V_0} = \sqrt{\frac{Z_{11}}{P_0}}C_y. \tag{A.41}$$

This result can be applied to the transformers on both the feed and coupled sides (M_f and M_c).

ACKNOWLEDGMENT

The author would like to acknowledge Dr. M. Adlerstein and Dr. F. Colomb, both of the Raytheon Company, Andover, MA, for their suggestion of this problem.

REFERENCES

[1] D. M. Pozar, "A microstrip antenna aperture coupled to a microstrip line," *Electron. Lett.*, vol. 21, pp. 49–50, Jan. 1985.
[2] ——, "A reciprocity method of analysis for printed slot and slot-coupled microstrip antennas," *IEEE Trans. Antennas Propagat.*, vol. AP-34, pp. 1439–1446, Dec. 1986.
[3] N. Herscovici and D. M. Pozar, "Full-wave analysis of aperture coupled microstrip lines," *IEEE Trans. Microwave Theory Tech.*, vol. 39, pp. 1108–1114, July 1991.
[4] C. Chen, M. J. Tsai, and N. G. Alexopoulos, "Optimization of aperture transitions for multiport microstrip circuits," *IEEE Trans. Microwave Theory Tech.*, vol. 44, pp. 2457–2465, Dec. 1996.
[5] K. Takeuchi, W. Chujo, and M. Fujise, "A slot coupled microstrip antenna with a thick ground plane," in *Eur. Microwave Conf. Dig.*, Sept. 1993.
[6] A. M. Tran and T. Itoh, "Analysis of microstrip lines coupled through an arbitrarily shaped aperture in a thick common ground plane," in *IEEE MTT-S Int. Microwave Symp. Dig.*, 1993, pp. 819–822.
[7] P. R. Haddad and D. M. Pozar, "Characterization of an aperture coupled microstrip patch antenna with a thick ground plane," *Electron. Lett.*, vol. 30, pp. 1106–1107, July 1994.
[8] M. Davidovitz, R. A. Sainati, and S. J. Fraasch, "A noncontact interconnection through an electrically thick ground plate common to two microstrip lines," *IEEE Trans. Microwave Theory Tech.*, vol. 43, pp. 753–759, Apr. 1995.
[9] P. R. Haddad and D. M. Pozar, "Analysis of two aperture coupled cavity-backed antennas," *IEEE Trans. Antennas Propagat.*, vol. 45, pp. 1717–1726, Dec. 1997.
[10] D. M. Pozar, *Microwave Engineering*, 2nd ed. New York: Wiley, 1998.
[11] C. A. Balanis, *Advanced Engineering Electromagnetics*. New York: Wiley, 1989.
[12] W. C. Chew and T. M. Habashy, "The use of vector transforms in solving some electromagnetic scattering problems," *IEEE Trans. Antennas Propagat.*, vol. AP-34, pp. 871–879, July 1986.

David M. Pozar (S'74–M'80–SM'88–F'90) received the Ph.D. degree from The Ohio State University, Columbus.

In 1980, he joined the faculty of the University of Massachusetts at Amherst. In 1988, he spent a sabbatical leave with the Ecole Polytechnique Federale de Lausanne, Lausanne, Switzerland. He has authored or coauthored over 100 papers on microstrip antennas and phased arrays. He also authored *Microwave Engineering, Second Edition* (New York: Wiley, 1997), *Microstrip Antennas* (Piscataway, NJ: IEEE Press, 1995), and *Microwave and RF Design of Wireless Systems* (New York: Wiley, 2000). He also authored *PCAAD*, a software package for personal computer-aided antenna design.

Prof. Pozar has served as an associate editor for the IEEE TRANSACTIONS ON ANTENNAS AND PROPAGATION (1983–1986 and 1989–1992), as a member of the IEEE Antennas and Propagation Society (IEEE AP-S) Administrative Committee (AdCom) (1989–1991), and as an associate editor of the *IEEE AP-S Newsletter* (1982–1984). He served as a Distinguished Lecturer for the IEEE AP-S from 1993 to 1995. He was the recipient of the 1981 Outstanding Professor Award presented by Eta Kappa Nu, the 1984 National Science Foundation (NSF) Presidential Young Investigator Award, the Keys to the Future Award presented by the IEEE AP-S, the 1985 University of Massachusetts Engineering Alumni Association Outstanding Junior Faculty Award, the 1986 R. W. P. King Best Paper Award presented by the IEEE AP-S, the 1987 URSI Issac Koga Gold Medal for his work on printed antennas and phased arrays, the 1988 R. W. P. King Best Paper Award, the 1989 United Technologies Corporation Outstanding Teaching Award, the 1995 College of Engineering Outstanding Senior Faculty Award, the 1997 College of Engineering College Outstanding Teacher Award, the 1998 H. A. Wheeler Applications Prize Paper Award presented by the IEEE AP-S, and a 2000 IEEE Third Millennium Medal.